

Deep reinforcement learning for flow control exploits different physics for increasing Reynolds-number regimes

Pau Varela¹, Pol Suárez^{2,3}, Francisco Alcántara-Ávila³, Arnau Miró², Jean Rabault⁴, Bernat Font², Luis Miguel García-Cuevas¹, Oriol Lehmkuhl² and Ricardo Vinuesa^{3*}

¹ CMT - Motores Térmicos, Universitat Politècnica de València, Spain

² Barcelona Super Computing Center - Centro Nacional de Supercomputación (BSC-CNS), Spain

³ FLOW, Engineering Mechanics, KTH Royal Institute of Technology, Stockholm, Sweden

⁴ Norwegian Meteorological Institute, Norway

* Correspondence: rvinuesa@mech.kth.se

Abstract: The current increase of emissions associated with aviation requires deeper research on novel sensing and flow-control strategies to obtain improved aerodynamic performance. In this context, data-driven methods are suitable for exploring new approaches to control the flow and develop more efficient strategies. Deep artificial neural networks (ANNs) used together with reinforcement learning, *i.e.* deep reinforcement learning (DRL), are receiving growing attention due to their capabilities to control complex problems in multiple areas. In particular, this technique has been recently used to solve problems related to flow control. In this work, an ANN trained through a DRL agent, coupled with the numerical solver Alya, is used to perform active flow control. The Tensorforce library is used to apply DRL to the simulated flow. Two-dimensional simulations of the flow around a cylinder are conducted and an active control based on two jets located on the walls of the cylinder is considered. By gathering information from the flow surrounding the cylinder, the ANN agent is able to learn through a proximal-policy optimisation (PPO) effective control strategies for the jets, leading to a significant drag reduction. Furthermore, the agent needs to account for the coupled effects of the friction- and pressure-drag components, as well as the interaction between the two boundary layers on both sides of the cylinder and the wake. In the present work, a Reynolds-number range beyond those previously considered is studied and compared with results obtained using classical flow-control methods. Significantly different nature in the control strategies is identified by the DRL as the Reynolds number Re increases. On one hand, for $Re \leq 1000$ the classical control strategy based on an opposition control relative to the wake oscillation is obtained. On the other hand, for $Re = 2000$ the new strategy consists of an energisation of the boundary layers and the separation area, which modulate the flow separation and reduce drag in a fashion similar to that of the drag crisis, through a high frequency actuation. A cross-application of agents is performed for a flow at $Re = 2000$, obtaining similar results in terms of drag reduction with the agents trained at $Re = 1000$ and 2000 . The fact that two different strategies yield the same performance make us question whether this Reynolds number regime ($Re = 2000$) belongs to a transition towards a nature-different flow which would only admit a high-frequency actuation strategy to obtain drag reduction. At the same time, this finding allows the application of ANNs trained at lower Reynolds numbers but comparable in nature, saving computational resources.

Keywords: numerical simulation; wake dynamics; flow control; machine learning; deep reinforcement learning



Citation: Varela, P. et al. Deep reinforcement learning for flow control exploits different physics for increasing Reynolds-number regimes. *Preprints* 2021, 1, 0. <https://doi.org/>

Received:

Accepted:

Published:

Publisher's Note: MDPI stays neutral with regard to jurisdictional claims in published maps and institutional affiliations.

1. Introduction

In transport applications and, especially, in aeronautics, drag reduction is directly related to a decrease in fuel use, which translates into reducing polluting and greenhouse-gas emissions [1]. Over the past decades, several techniques have been developed and used to reduce

drag, both passively (Bechert and Bartenwerfer [2]) and actively (Gad-el Hak [3]). Passive methods typically rely on fixed geometric changes without using actuators. An example of this technology would be the widespread use of winglets in aircraft. Inspired by bird wings, winglets consist of small wing extensions at the wing tip with an angle relative to the wing-span direction. Using winglets, lift-induced drag is decreased by reducing the size and formation of vortices at the wing tip [4], incurring in (hopefully) small increases in structural weight and parasitic drag. Regarding active methods, diverse techniques are used to reduce aircraft drag and associated emissions. In the work of Tiseira *et al.* [5] and Serrano *et al.* [6,7], the use of distributed electric propulsion is combined with boundary-layer ingestion, setting small propellers along the wing near the trailing edge. Thanks to both technologies, it is possible to increase the aerodynamic efficiency of small aircraft or unmanned air vehicles (UAVs). In the same way, the location and use of both jet pumps in wings and synthetic jets are studied to reduce the drag of different aerodynamic bodies. An example of blowing and suction used to control turbulent boundary layers is provided by Kametani and Fukagata [8], and a number of studies have shown the feasibility of this approach in turbulent wings [9–12].

Additional examples can be found in the the work of Voevodin *et al.* [13] and Yousefi and Saleh [14], where the placement of suction and ejection in wing airfoils is studied to reduce aerodynamic drag or achieve efficient control of the flow around the wing in specific flight-operating conditions. In the same way, the use of synthetic jets has been studied to achieve this same objective, as displayed in the work of Cui *et al.* [15] on an Ahmed body, or the investigation of Park *et al.* [16] using an array of synthetic jets applied to a car. A comprehensive review of active flow control in turbulent flows is provided by Choi *et al.* [17].

Active-control methods rely on complicated control strategies due to their variable behaviour and dependencies. As shown by Muddada and Patnaik [18], even the control of simple actuators to reduce the drag of a cylinder immersed in a low-Reynolds-number flow can be complicated due to the interaction between boundary layers, separating shear layers and wake. In this case, by correctly developing a control algorithm, the drag is reduced by about 53 %, leaving ample room for improvement in the case of achieving better control. However, thanks to the application of artificial neural networks (ANNs) and deep reinforcement learning (DRL), it is possible to develop functional control strategies at an affordable computational cost in similar problems, as shown by the work by Rabault *et al.* [19]. An ANN is a non-parametric tool formed by layers of connected processing nodes or neurons and it can be trained to solve complex problems [20,21]. The ANN training can take place through different types of learning, where DRL is one of the fastest-growing in solving a wide range of cases [22,23], including flow control in complex geometries [24,25].

DRL is based on maximising a reward by means of an agent interacting with the environment through actions, based on partial observations of the environment. Note that the combination of DRL and ANN was successfully carried out to solve active flow control in the work of Rabault *et al.* [19]. A proximal-policy-optimisation (PPO) is used to obtain the control policy of two synthetic jets on a two-dimensional cylinder in a low-Reynolds-number flow. PPO parameterises a policy function using an ANN with a set of neuron weights given an observation state. The ANN then produces a set of moments that describe a distribution function from which actions are sampled. It is possible to obtain an expression for the estimation of the gradient of the reward as a function of the neuron weights. Additionally, the PPO uses a critic network that estimates the new reward function, which is helpful with stochastic data. Also, there is a limit in the maximum update at every training step, preventing rare events from producing a large reward [26]. It was shown that DRL was feasible and enabled finding a control strategy such that the cylinder drag was reduced by 8 %. Rabault and Kuhnle [27] developed a framework to parallelise environments, enabling speeding up computation and learning, thus reaching a better solution faster. Additionally, Tang *et al.* [28] validated

the DRL approach in a more complex problem using four jets on the cylinder and extending the Reynolds-number range. The results of Rabault *et al.* [19,27] have been extended by a multitude of studies in recent years. For example, the works of Tokarev *et al.* [29] or Xu *et al.* [30], where an oscillatory rotary control is applied to the cylinder; the study of linear stability and low sensitivity that allows a better understanding of DRL by Li and Zhang [31], or the effort of Ren *et al.* [32] where the same DRL approach is used with a solver that allows calculations at higher Reynolds numbers, with the additional problem of controlling the increase in turbulence around the cylinder. Applications to square cylinders, which are relevant to civil engineering, have also been presented recently [33], as well as using traditional modal analysis methods for defining effective reward functions [34]. Regarding these works, there is room for improvement through the application of high-performance computing (HPCs), enabling conducting faster calculations at higher Reynolds numbers not previously calculated.

The main objective of this work is, indeed, to demonstrate the capabilities of the HPC resources available today to perform aerodynamic optimisation with DRL-based control at much higher Reynolds numbers than the ones already studied in the literature. This project proposes the use of the numerical code Alya, developed in the Barcelona Supercomputer Center (BSC-CNS) [35], employing the HPC Marenostrum IV cluster. Alya is a tier-0 massively parallel code and is designed to solve the discretised partial differential equations using finite elements. This code has been successfully used in different problems of fluid mechanics, including simulations of turbulent flows [36,37].

In the present work, the methodology is first detailed in [section 2](#), dedicated to the numerical setup and the application of the DRL and the ANN. The results are then summarised and discussed in [section 3](#), which starts with the validation of the Alya solver in the combination of an HPC cluster to solve the DRL problem in the cylinder. Then, the results derived from the increase in Reynolds number, which exceed the conditions reported in the literature, are shown. Finally, the main conclusions are collected in [section 4](#).

2. Methods

This section is divided into two parts: the problem description and the domain setup along the methodology regarding the numerical simulations; and the framework including the DRL algorithm.

2.1. Problem configuration and numerical setup

The domain simulation is two dimensional (2D) and consists of a cylinder immersed in a rectangular channel, in the same configuration as that described in the work by Rabault *et al.* [19]. The domain is normalised using a cylinder with diameter D as the reference length scale. The channel has a dimension of $L = 22$ in length, aligned with the main flow direction, and a height equal to $H = 4.1$. The origin of the coordinate system is set on the left-bottom corner of the channel, and the center of the cylinder displaced towards the bottom by $0.05D$ units, to develop the vortex-shedding behind it. A schematic representation of the domain is depicted in [Figure 1](#). Aligned with the vertical axis and symmetrically on the cylinder wall, one at the top and one at the bottom, there are two synthetic jets with a total opening of $\omega = 10^\circ$ each. This position of the jets is chosen so their actuation is normal to the flow and drag reduction comes from effective actuation rather than injection of momentum.

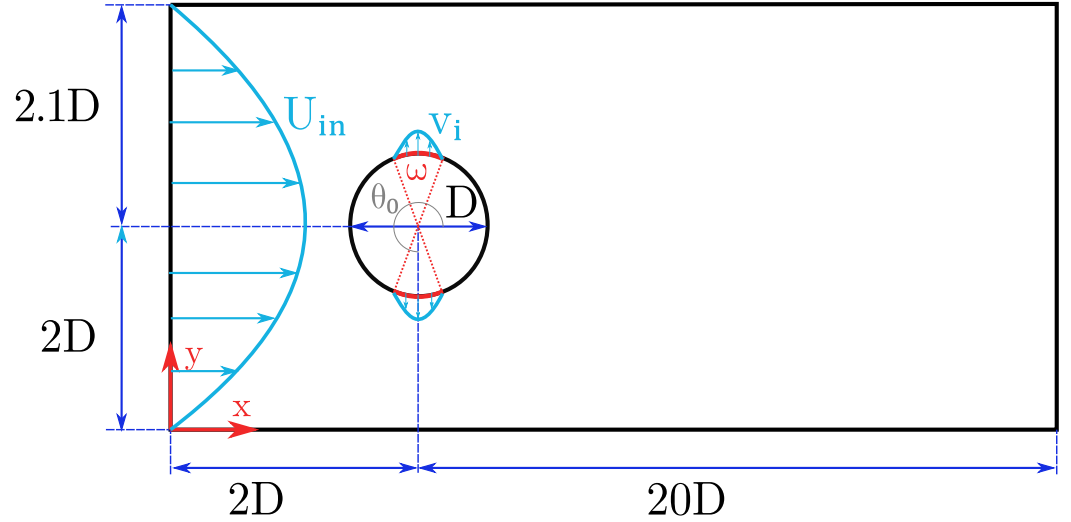


Figure 1. Main domain dimensions in terms of the cylinder diameter D , where ω represents the jet width and θ_0 is the angle of the center of the jet. In light blue the parabolic velocity profile of the inlet and the jet are represented. The domain representation is not to scale.

Regarding the boundary conditions of the problem, an inlet parabolic velocity condition is imposed and expressed as in Equation 1:

$$U_{\text{in}}(y) = U_{\text{max}} \left[1 - \left(2 \frac{y - H/2}{H} \right)^2 \right], \quad (1)$$

where $[U_{\text{in}}(y), V_{\text{in}}(y) = 0]$ is the velocity vector and U_{max} is the maximum velocity reached at the middle of the channel, which is equal to 1.5 times the mean velocity \bar{U} , defined as shown in Equation 2:

$$\bar{U} = \frac{1}{H} \int_0^H U_{\text{in}}(y) dy = \frac{2}{3} U_{\text{max}}. \quad (2)$$

A value of $U_{\text{max}} = 1.5$ is used so that the scaling velocity of the problem is $\bar{U} = 1$. A no-slip condition is imposed on the cylinder solid wall, while a smooth-wall condition is imposed on the channel walls. The right boundary of the channel is set as a free outlet with zero velocity gradient and constant pressure. The jet velocity (v_i) is a function of both the set jet angle (θ) and the mass flow rate (Q) determined by the ANN, as described in Equation 3:

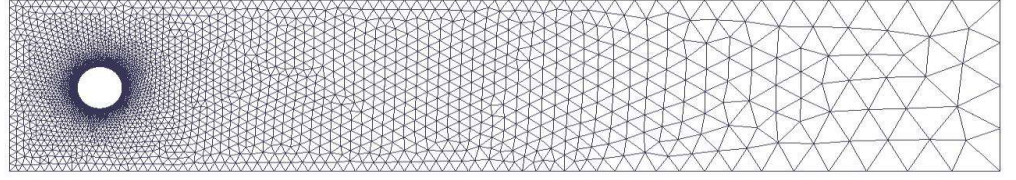
$$v_i = Q \frac{\pi}{2\omega R^2} \cos \left[\frac{\pi}{\omega} (\theta - \theta_0) \right], \quad (3)$$

where θ_0 corresponds to the angle where the jet is centred and R is the cylinder radius. The scaling factor $\pi/(2\omega R^2)$ is used so that the integration of the jet velocity over the jet width gives the desired mass flow rate Q . More details about the intensity parameters are provided in subsection 2.2.

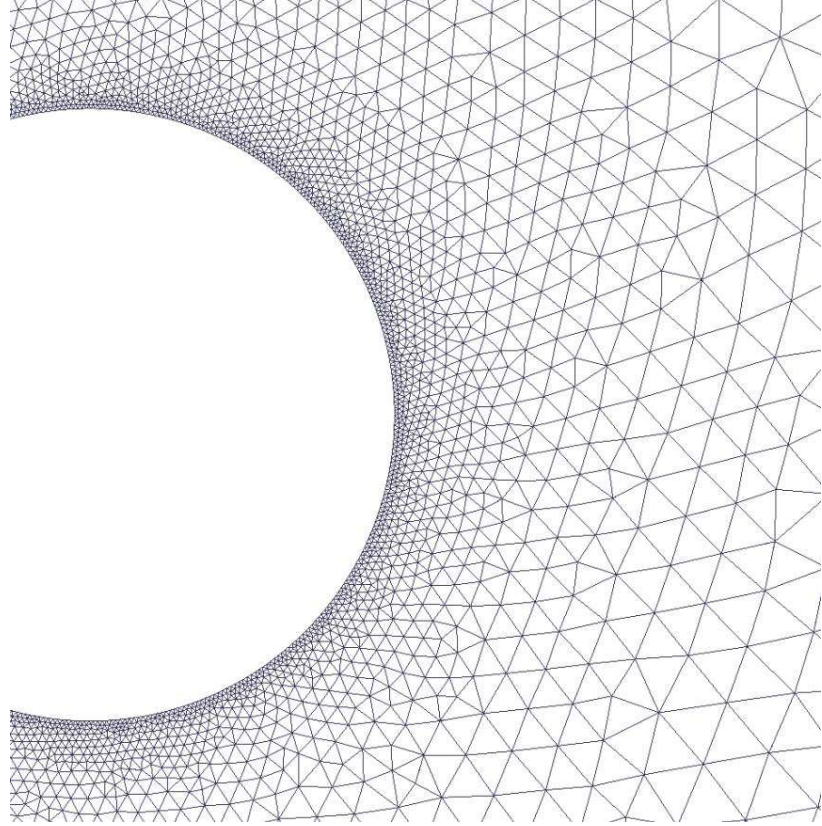
Re	100	1000	2000
Mesh cells (approx.)	11000	19000	52000
Number of witness points	151	151	151
$ Q _{\max}$	0.088	0.04	0.04
s_{norm}	1.7	2	2
C_{offset}	3.17	3.29	3.29
r_{norm}	5	1.25	1.25
w	0.2	1	1
T_k	3.37	3.04	4.39
T_a	0.25	0.2	0.2
Actions per episode	80	100	100
Number of episodes	350	1000	1400
CPUs per environment	46	46	46
Environments	1	1 or 20	20
Total CPUs	46	46 or 920	920
Baseline duration	100	250	100

Table 1: Parameters of the simulations for each Reynolds number considered in this work.

The Reynolds number $Re = \overline{U}D/\nu$ of the simulation is varied between 100, 1000 and 2000, where ν is the fluid kinematic viscosity. For the mesh, an unstructured mesh of triangular elements with refinement near the cylinder wall and the jets has been used, as shown in [Figure 2](#). The number of elements changes with the Reynolds number as expressed in [Table 1](#).



(a) Unstructured triangular mesh employed in all the domain.



(b) Detailed mesh around the cylinder.

Figure 2. Computational grid used for the $Re = 100$ calculations.

Alya is used to simulate the flow. This solver assumes that the flow is viscous and incompressible, where the governing Navier–Stokes equations can be written for a domain Ω as in [Equation 5](#):

$$\partial_t \mathbf{u} + (\mathbf{u} \cdot \nabla) \mathbf{u} - \nabla \cdot (2\nu \boldsymbol{\epsilon}) + \nabla p = \mathbf{f} \quad \text{in } \Omega \in (t_0, t_f), \quad (4)$$

$$\nabla \cdot \mathbf{u} = 0 \quad \text{in } \Omega \in (t_0, t_f), \quad (5)$$

where $\boldsymbol{\epsilon}$ is a function of the velocity \mathbf{u} which defines the velocity strain-rate tensor ($\boldsymbol{\epsilon} = 1/2(\nabla \mathbf{u} + \nabla^T \mathbf{u})$) and \mathbf{f} are the external body forces. In [Equation 4](#), the convective form of the nonlinear term, $\mathbf{C}_{\text{nonc}}(\mathbf{u}) = (\mathbf{u} \cdot \nabla) \mathbf{u}$, is expressed as a term conserving energy, momentum and angular momentum [38,39]. This form is known as EMAC (energy-, momentum- and

angular-momentum-conserving equation), and its expression appears in equation [Equation 6](#). The EMAC form ([Equation 6](#)) adds to the equation the conservation of energy as well as linear and angular momentum at the discrete level:

$$C_{\text{emac}} = 2\mathbf{u} \cdot \boldsymbol{\epsilon} + (\nabla \cdot \mathbf{u})\mathbf{u} - \frac{1}{2}\nabla|\mathbf{u}|^2. \quad (6)$$

The spatial discretisation of the Navier-Stokes equations is performed by means of the finite-element method (FEM). Meanwhile, the time discretisation uses a semi-implicit Runge–Kutta scheme of second order for the convective term, and a Crank–Nicolson scheme for the diffusive term [40]. In the time integration, Alya uses an eigenvalue time-step estimation as described by Trias and Lehmkuhl [41]. The complete formulation of the flow solver is described in the work by Lehmkuhl *et al.* [37].

At each time step, the numerical solution is obtained and the drag F_D and lift F_L forces are integrated over the cylinder surface \mathbf{S} as follows ([Equation 7](#)):

$$\mathbf{F} = \int (\boldsymbol{\zeta} \cdot \mathbf{n}) \cdot \mathbf{e}_j d\mathbf{S}, \quad (7)$$

where $\boldsymbol{\zeta}$ is the Cauchy stress tensor, \mathbf{n} is the unit vector normal to the cylinder and \mathbf{e}_j is a unit vector in the direction of the main flow velocity when calculating the drag and a vector perpendicular to the velocity of flow for the calculation of the lift force. The drag C_D and lift C_L coefficients are computed as described in [Equation 8](#) and [Equation 9](#):

$$C_D = \frac{2F_D}{\rho \bar{U}^2 D}, \quad (8)$$

$$C_L = \frac{2F_L}{\rho \bar{U}^2 D}. \quad (9)$$

2.2. DRL setup

As discussed in the introduction, the DRL interacts with the domain through three channels. The first channel is the observation state (s), based on the extraction of pressure values at a series of predefined points along the domain. These points, known as witness points or probes, are located in the same positions as in Rabault *et al.* [19]. There are 151 witness points in total distributed around the cylinder and along the wake as shown in [Figure 3](#). The values of the pressure obtained at the witness points are normalised by a factor s_{norm} so that the state values given to the agent are between -1 and 1 , approximately. The values of s_{norm} for each Reynolds-number case are given in [Table 1](#).

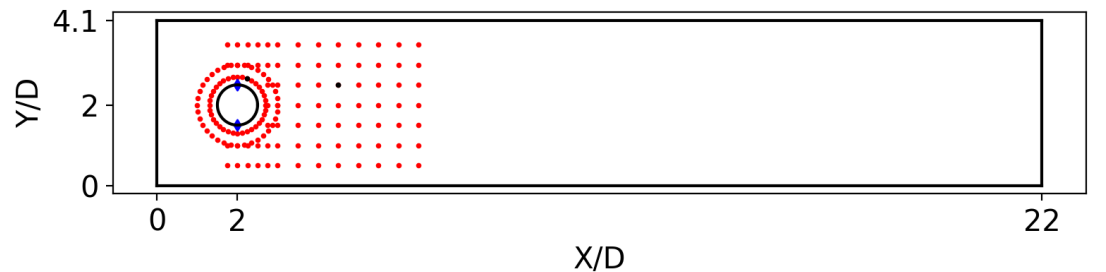


Figure 3. Schematic representation of the computational domain, where the red dots correspond to the location of the probes. The position of two probes is remarked as black dots for further analysis in [subsection 3.3](#).

The second channel of interaction between the DRL and the numerical simulation is the action that is given by the control of the jets on the cylinder (a). The value of the action a is directly related with the control value of the upper jet intensity Q_1 , while the bottom jet will do the opposite control to ensure a global zero mass flow rate between both jets, i.e. $Q_2 = -Q_1$. This is a more realistic control and helps to make the numerical scheme more stable as reflected by Rabault *et al.* [19]. During the training, the maximum value of $|Q_1|$ is limited to $|Q_1| < 0.06 Q_{\text{ref}} \approx 0.88$ for the $Re = 100$ case, as in the work by Rabault *et al.* [19], to avoid unrealistically large actuations. Note that Q_{ref} is the mass flow rate intercepting the cylinder, and it is calculated as in Equation 10:

$$Q_{\text{ref}} = \int_{-D/2}^{D/2} \rho U_{\text{in}}(y) dy. \quad (10)$$

For higher Reynolds numbers this clipping value of $|Q_1|$ is reduced to 0.04. In addition, even though the value of Q selected by the ANN is unique in each action, Q is not imposed as a constant value during the entire action duration. In particular, Q is assessed as a curve to prevent significant changes in the boundary condition between actions that could lead to numerical discrepancies, similar to how the smooth control was presented by Tang *et al.* [28]. This way, the imposed mass flow starts from the previous value Q_0 and increases or decreases linearly until the new value Q_1 has been achieved during the entire action time $T_a = t_1 - t_0$. Consequently, Q in Equation 3 is presented as a function of time in Equation 11 and is illustrated in Figure 4.

$$Q(t) = \frac{Q_1 - Q_0}{T_a} (t - t_0) + Q_0. \quad (11)$$

It should be noted that the first action of each episode (an episode is understood as a sequence of interactions between the neural network and the simulation, which generates the input data for the agent algorithm) always starts from a baseline case, i.e. a periodically stable flow without jet actuation. This baseline case uses the same domain, and the flow is fully developed without applying jet control.

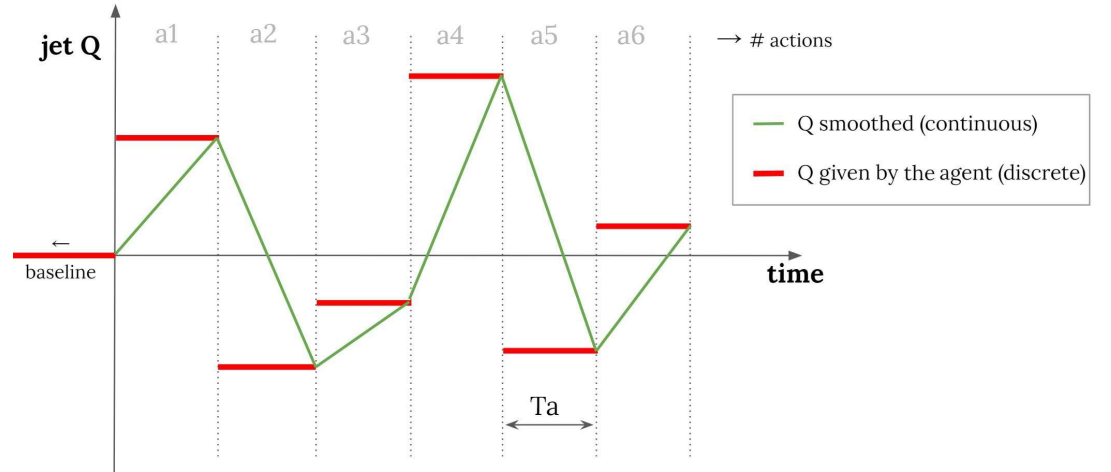


Figure 4. Flow rate of the jet Q smoothed and applied in the numerical simulation (green) versus the discrete Q decided by the DRL agent (red).

The third interaction channel between the DRL and the numerical simulation is the reward or goal (r), which in this case is aimed at minimising the cylinder drag and it is defined as in Equation 12:

$$r = r_{\text{norm}}(-\langle \overline{C_D} \rangle - w\langle \overline{C_L} \rangle + C_{\text{offset}}), \quad (12)$$

where $\langle \cdot \rangle$ indicates averaging over a baseline vortex-shedding period, w is a lift-penalisation factor, C_{offset} is a coefficient to centre the initial reward around 0, obtained from the value of r at the end of the baseline simulation, and r_{norm} is used to normalise this reward between 0 and 1 approximately. In such a way, the agent receives the reward in an optimal range. Note that the value of r_{norm} is set from an a priori guess of the expected the maximum reward. The lift-penalisation factor is set in such a way that the drag is minimised, and at the same time the effect of the possible growth of induced lift is mitigated. If this lift penalisation is not introduced into the reward function, the agent can find a strategy where both jets blow in the same direction at their maximum strength, as discussed in Rabault and Kuhnle [27]. The values of w , C_{offset} and r_{norm} are given in Table 1 for the different Reynolds numbers.

In a nutshell, the agent will choose an action (a) given a specific state (s) in order to maximise a reward (r). The function that determines what will be the reward is a normal distribution. During the training process, the agent will choose an action around the average of this normal distribution. This is known as the exploration noise and it helps the method to converge towards a better solution. Once the training has been performed, the agent can be tested in a deterministic mode. Here, the most probable action in the normal distribution is chosen in order to maximise the reward with the learning obtained during the training.

Following the work by Rabault *et al.* [19], the ANN is designed with two dense layers of 512 neurons and a PPO agent is selected to carry out the control. The PPO agent follows a policy-gradient method in order to obtain the weights of the ANN. The implementation of the DRL is done through the open-source Tensorforce library [42], which is built from the TensorFlow open-source library [43], and it includes defining and creating both the ANN and the control agent. The selection of the initial parameters of the DRL depends intrinsically on the problem itself. In this case, the total number of actions is related to the vortex-shedding period $T_k = 1/f_k$ through the Strouhal number $St = f_k \cdot D/\bar{U}$.

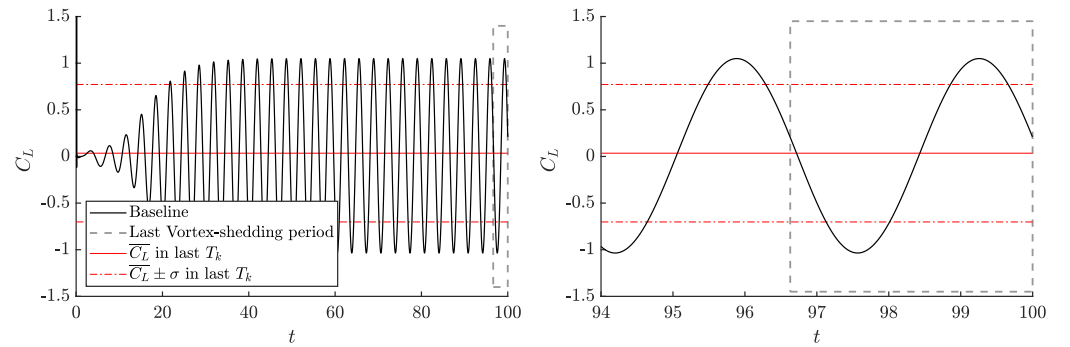


Figure 5. Temporal evolution of the lift coefficient in the baseline case (without jet actuation). (a) Baseline lift-coefficient results. The vortex-shedding period is 3.37 time units. (b) Zoom-in view of the vortex-shedding period in the baseline case.

Figure 5 shows the lift coefficient of the baseline case. This figure shows that the vortex-shedding period is $T_k = 3.37$ time units for the $Re = 100$ case and $St = 0.29$; this is in agreement with both experiments [44] and simulations [19]. Taking the vortex-shedding period as reference, the action time T_a is defined as 7.5 % of T_k , as in Rabault *et al.* [19]. This period of actuation was found to be large enough so the consequences of the actuation can be perceived by the flow, and small enough so that the actuations can anticipate and adapt to the needs of the control. In the higher- Re cases, this actuation period is reduced to $T_a = 0.2$

due to their more chaotic flow behaviour and, therefore, the necessity to adapt the actuations faster. Based on this simulation, it can be concluded that before starting the DRL, the baseline case needs to be run for over 50 time units in order to obtain a periodic stabilised flow. As suggested in the work of Rabault *et al.* [19], at $Re = 100$ the typical time of an episode should be between 6 and 8 vortex sheddings so that the agent has enough time to learn the suitable control policy. A total of 80 actuations are carried out on each episode, resulting in an episode duration of 20 time units. In the case of higher Reynolds number, a total of 100 actions are conducted in each episode, since the duration of each actuation is reduced.

For the cases at high Reynolds number of 1000 and 2000 parallel environment framework has been adopted to speed up the learning process using a total of 20 environments. Also, in the case at $Re = 1000$ a comparison of the results is done when a single environment is employed. A total of 46 Marenstrum IV central-processing units (CPUs) are used on each environment. Therefore, a total of 46 or 920 CPUs are used depending on whether a single environment or 20 environments are considered on the case, respectively. All these parameters are collected in Table 1. The general DRL framework is summarised in Figure 6.

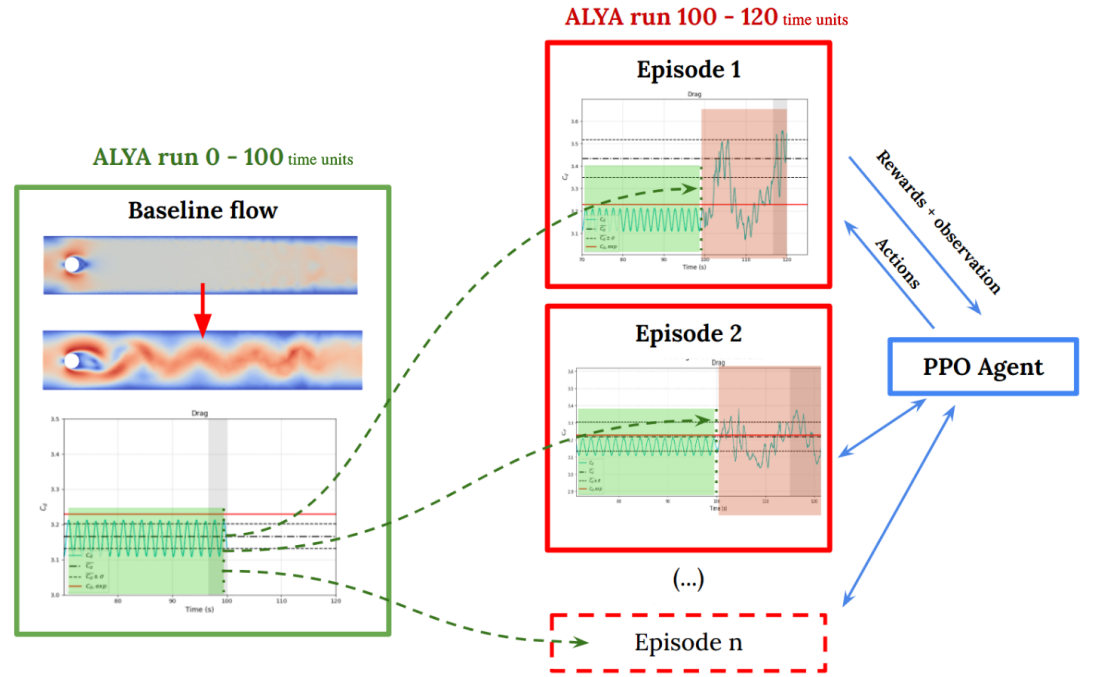


Figure 6. General overview of the DRL-CFD (computational fluid dynamics) framework employed in this work. A multi-environment approach is used to parallelise the learning and to speed up training.

3. Results and discussion

This section is divided into three parts. First, the results obtained using the Alya solver and the DRL applied are validated using literature data. Once validated, higher Reynolds number results are obtained and discussed, for which no precedent has been found in the literature. Finally, a cross-application of agents is analysed to save computational resources in resolving cases with high Reynolds numbers.

3.1. CFD and DRL code validation

As can be seen in the work by Rabault *et al.* [19] for a $Re = 100$, through the correct actuation of the DRL, it was possible to achieve a decrease in cylinder drag of 8 %. These

results have been validated in other simulations, such as Li and Zhang [31], and applied in similar research [29,45,46].

Figure 7 shows eleven different trainings launched and the average C_D obtained for the last vortex-shedding period of the different episodes. It can be seen that all cases follow the same learning trend, where most of the said learning is observed in the first hundred episodes. The main trend is obtained by adjusting a fourth-degree polynomial fit using the average coefficient data, and its purpose is to help to visualise the data. From this point on, the slope of the C_D decrease is not so pronounced, reaching a stable solution for 350 episodes.

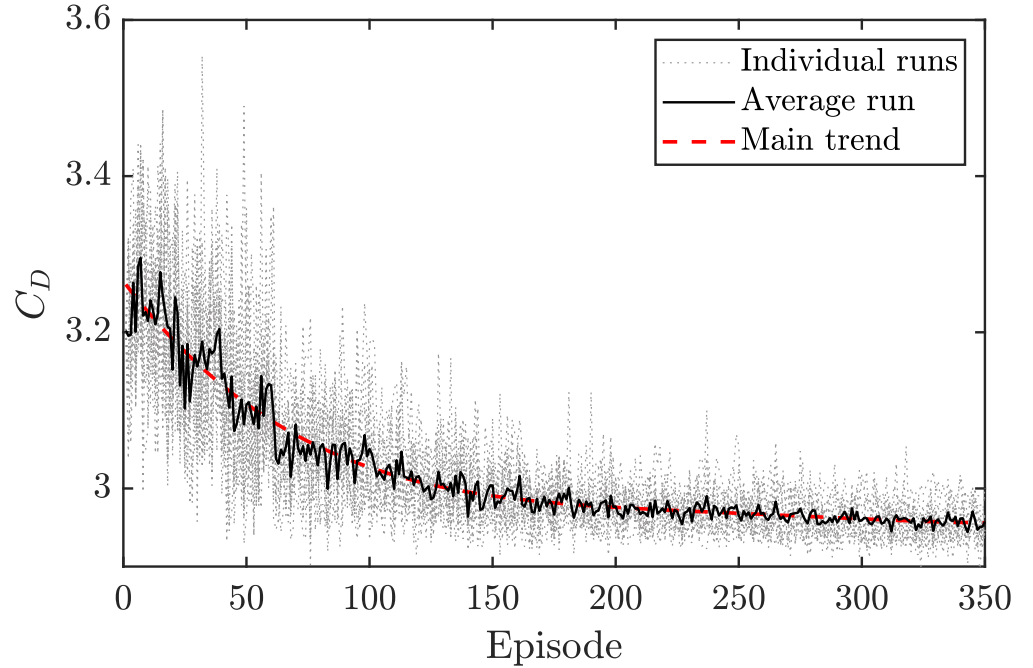


Figure 7. Evolution of C_D in the last vortex-shedding period as a function of the episode.

The obtained learning is then applied to the previously-shown baseline. To this end, one of the 11 trained agents is randomly selected and is run in a deterministic mode. This deterministic simulation is initiated from the conditions of the baseline case at 100 time units from the start. The C_D and C_L trends are shown in Figure 8, which indicates that a value of $C_D = 2.95$ is obtained after applying the control, *i.e.* a decrease of 8.9% compared with the baseline case. The C_D improvement is calculated as a function of the baseline C_D :

$$\text{improvement} = \left[1 - \frac{C_D^{\text{controlled}}}{C_D^{\text{baseline}}} \right] \times 100. \quad (13)$$

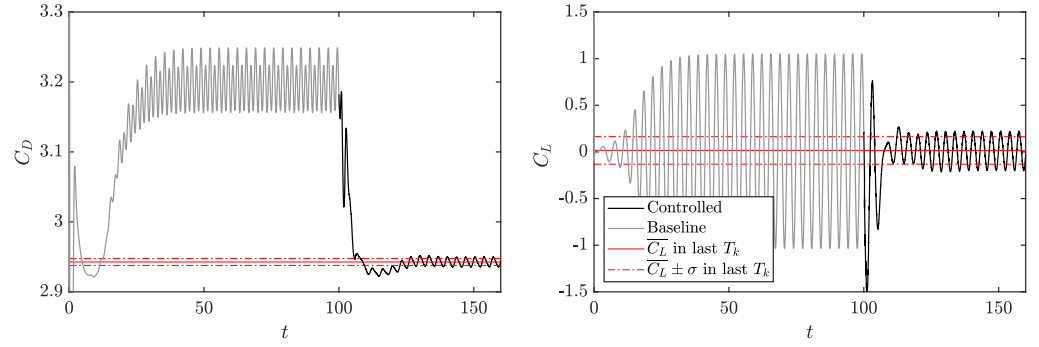


Figure 8. Temporal evolution of C_D (left) and C_L (right) obtained through the application of the DRL control (at $t = 100$), run in a deterministic mode, for $Re = 100$.

This result is rapidly achieved from the moment the control is applied. In the case of C_L , the mean remains approximately at 0. However, the amplitude of the variation of this coefficient has been reduced, as shown by the lower standard deviation obtained. This may indeed have great beneficial consequences from the structural and stability points of view.

The control imposed on each jet is represented in Figure 9. As discussed above, the control starts at 100 time units of simulation, so the values of injected or suctioned mass prior to this time are null. Having imposed the synthetic-jet condition, everything injected by one jet (positive values) will be equivalent to what is suctioned by the other (negative values). In the first 10 time units approximately, the control of greater amplitude leads to a significant reduction in the drag, maximising the reward. Next, a transitional control seeks to obtain a more stable actuation. After 25 time units, the solution is practically periodic.

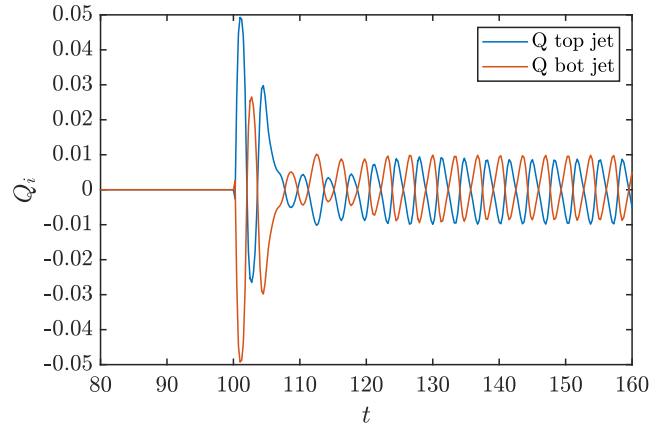
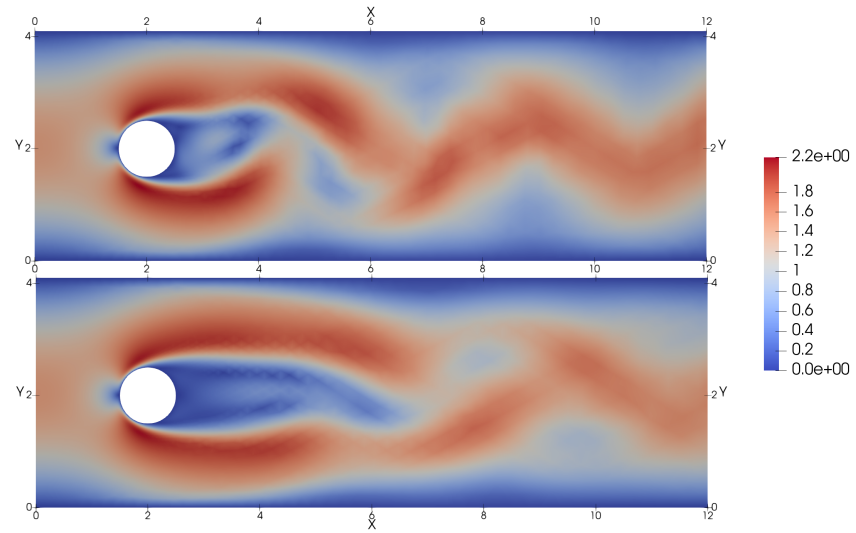
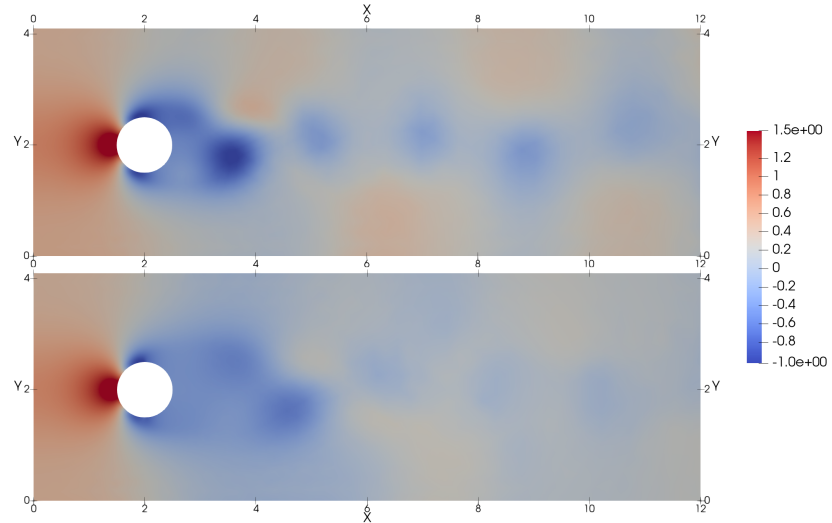


Figure 9. Flow rate through each jet as a function of time after applying the DRL control.

More information about the control is obtained by observing the contours of instantaneous velocity and pressure for the controlled and uncontrolled cases, as shown in Figure 10. The DRL agent reduces C_D by manipulating the wake vortex: it increases the size of the recirculation region and reduces both the frequency and the amplitude of the von Kármán street downstream of the cylinder. A similar conclusion is obtained from the instantaneous pressure field, which exhibit a decrease in the pressure maxima after applying the control. Comparing our results with those by Rabault *et al.* [19], it can be seen that the response of the control is practically the same except for very small differences that can come from the different numerical schemes to resolve the flow.



(a) Instantaneous velocity-magnitude fields.



(b) Instantaneous pressure fields.

Figure 10. Instantaneous flow fields at $Re = 100$, where for each pair of images, the baseline case without control is depicted on the top and the controlled case is depicted on the bottom.

Increasing the Reynolds number also requires reducing the period of actuation, as mentioned in [subsection 2.2](#). Additionally, increasing the Reynolds number leads to a more complex flow, thus a higher number of episodes are expected to be necessary to complete the training. Therefore, parallelisation using 20 environments has been adopted when simulating higher- Re cases. The parallelisation using a multi-environment approach is fully detailed in the work of Rabault and Kuhnle [27].

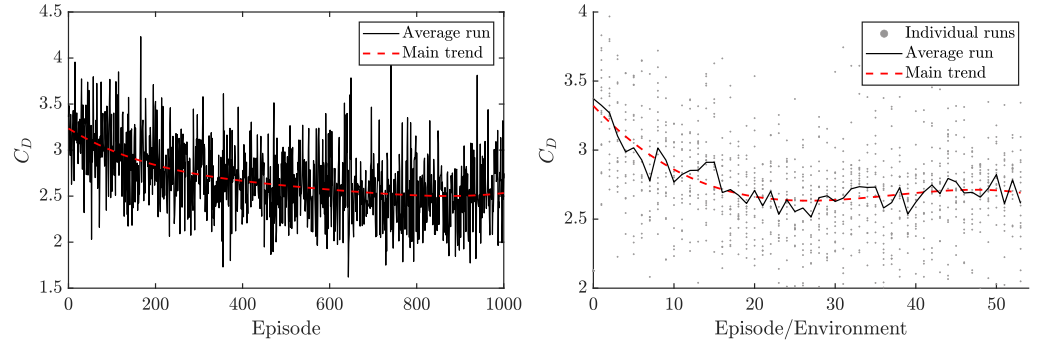


Figure 11. Evolution of C_D in the last vortex-shedding for each episode employing a single environment (left) or a 20-multi-environment approach (right) showing the learning curve indexed by the episode number for one of the 20 environments.

In Figure 11, a comparison between employing a single environment and a 20 multi-environment approach is conducted for a case of $Re = 1000$. It can be observed that if the Reynolds increases an order of magnitude, in this case, the number of episodes for the DRL to act to the same degree is three times greater using only one environment, as compared with Figure 7. The same solution can be obtained by parallelising through 20 environments, using 50 episodes in each environment, which helps to reduce the real calculation time significantly.

As mentioned before, the flow is more complex, and its structures are less periodic and more chaotic. To analyse the flow, the instantaneous and average velocity field are represented in Figure 12.

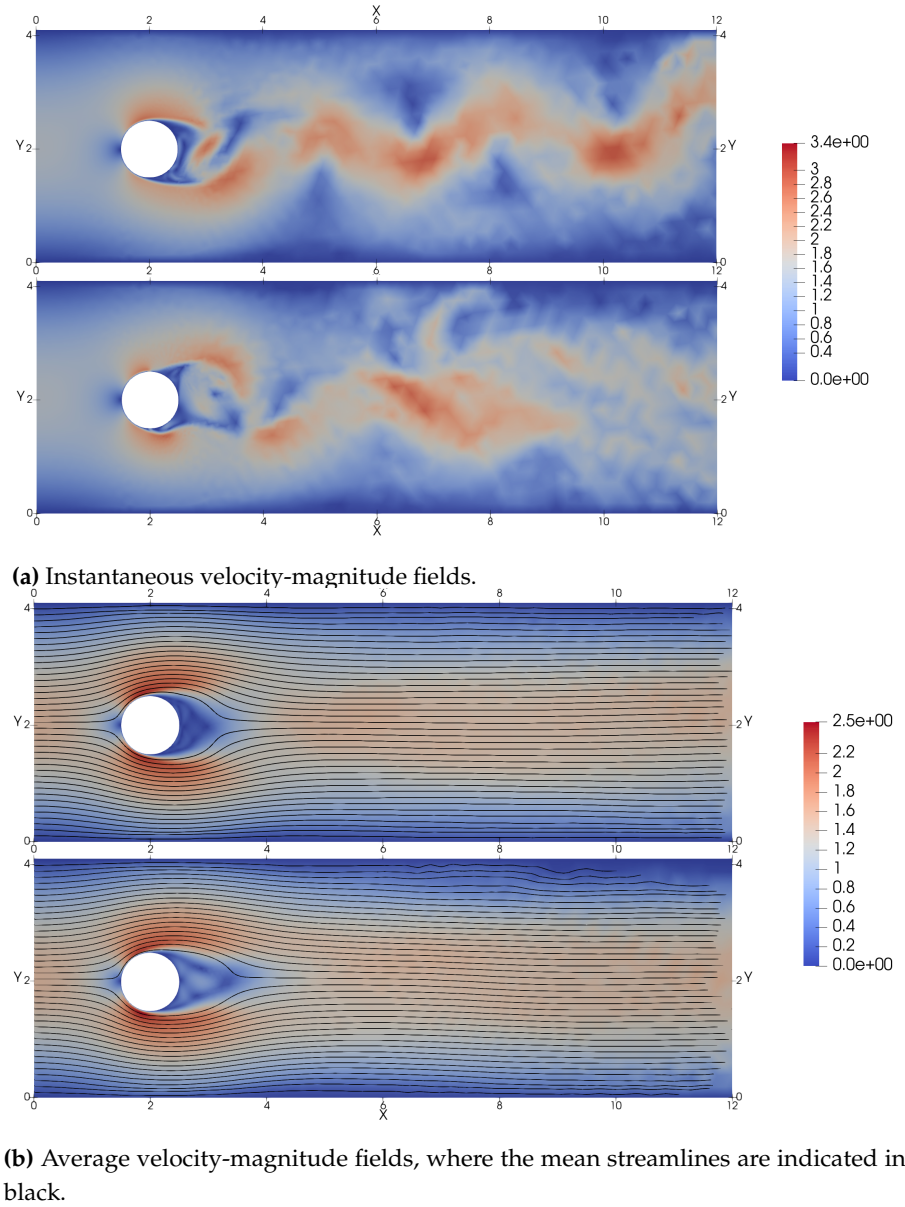


Figure 12. Instantaneous and average flow fields at $Re = 1000$, where for each pair of images, the baseline case without control is depicted on the top and the controlled case is depicted on the bottom.

The obtained results are consistent with those of Ren *et al.* [32], which reports an extensive flow analysis of the same Reynolds number. The control produces an elongation of the recirculation bubble behind the cylinder, reducing at the same time the hydrodynamic drag. For this Reynolds number, the control strategy found by the PPO agent is based on synchronous blowing. This strategy is similar to that found in lower Reynolds numbers: the jets produce an ejection or suction, generating a flow opposite to that caused by the wake.

3.2. DRL application at Reynolds number 2000

Through the use of parallelisation with a multi-environment strategy, even higher Reynolds numbers can be achieved. The results obtained for a training with $Re = 2000$ are discussed below and, to the authors' knowledge, there is no record of applying DRL control to such a high Reynolds number in the literature.

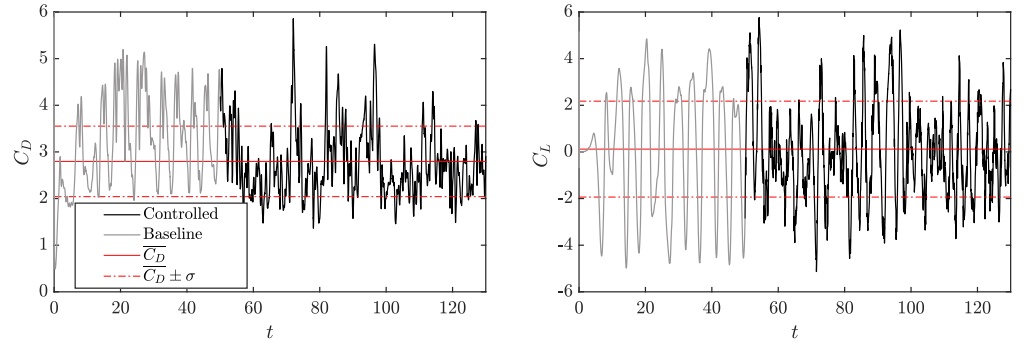
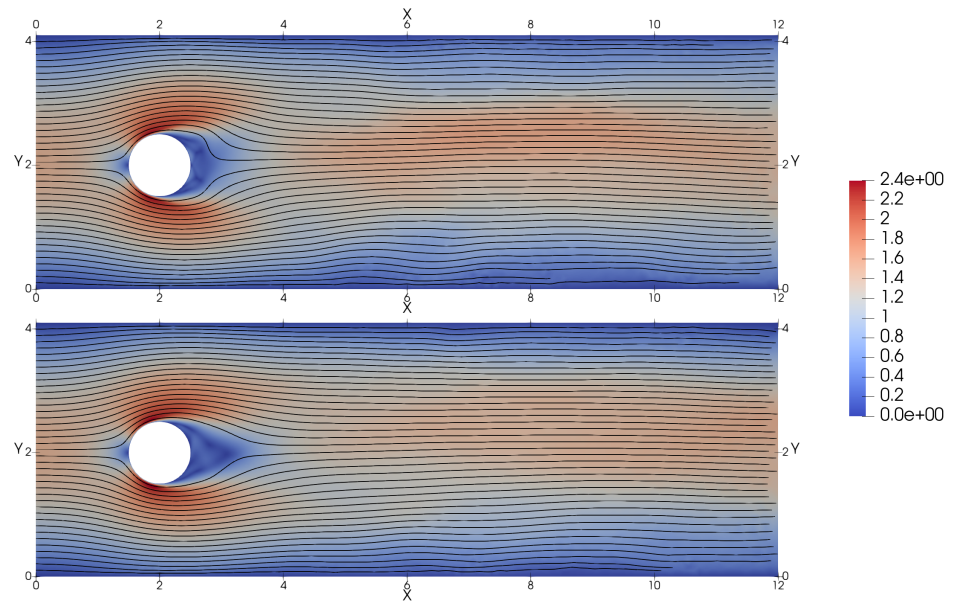


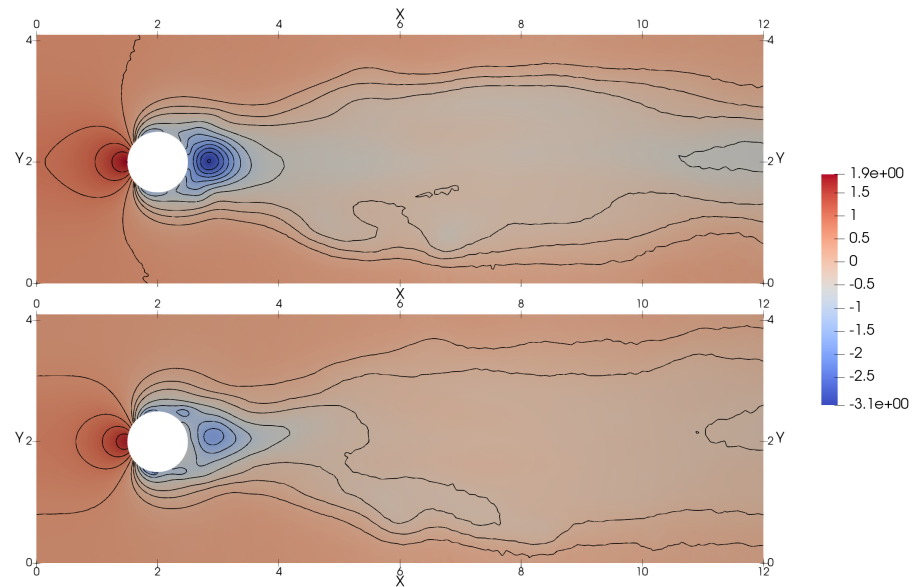
Figure 13. Temporal evolution of C_D (left) and C_L (right) obtained through the application of the DRL control (at $t = 50$), run in a deterministic mode, for $Re = 2000$.

The C_D and C_L obtained through the application of the learning in a deterministic mode is represented in Figure 13. This figure contrasts sharply with the one observed with $Re = 100$ (Figure 8). In this case, the starting baseline flow is much more chaotic, which can be seen in the magnitude of the peaks of both variables. The average drag coefficient of the non-controlled flow is $C_D = 3.39$. After the control, the average in this period is $C_D = 2.79$, which means more than 17% of C_D improvement. In this case, it has been chosen to represent the mean in the entire controlled period and not during the last vortex-shedding since, as the solution behaves more erratically, it could lead to an average that is far from reality. Regarding the lift coefficient, the applied control manages to set the average C_L with a close value to 0, maximising the reward function as desired and avoiding a systematic biased strategy (see Appendix B in Rabault and Kuhnle [27]). Also the absolute value of the peaks during the oscillating periods is reduced but not as much as in the case at Reynolds number 100, due to the chaotic nature of the flow at this higher Reynolds number.

In Figure 14 the average velocity and pressure fields are shown both for the baseline and the controlled deterministic case. As can be seen in the average velocity field comparison, the separation point in the controlled case is further downstream of the cylinder. This way, the average wake is narrowed faster in the controlled case, lowering the drag produced. This phenomenon is easier to observe if the difference between the baseline and the controlled case is considered as shown in Figure 15. This figure shows that the more significant difference between the controlled and uncontrolled cases occurs in the separation zone. At the same time, as observed for lower-Reynolds-number control, the pressure drop behind the cylinder is reduced when controlled.



(a) Average velocity-magnitude fields.



(b) Average pressure fields.

Figure 14. Average flow fields at $Re = 2000$, where each pair of images, the baseline case without control is depicted on the top and the controlled case is depicted on the bottom.

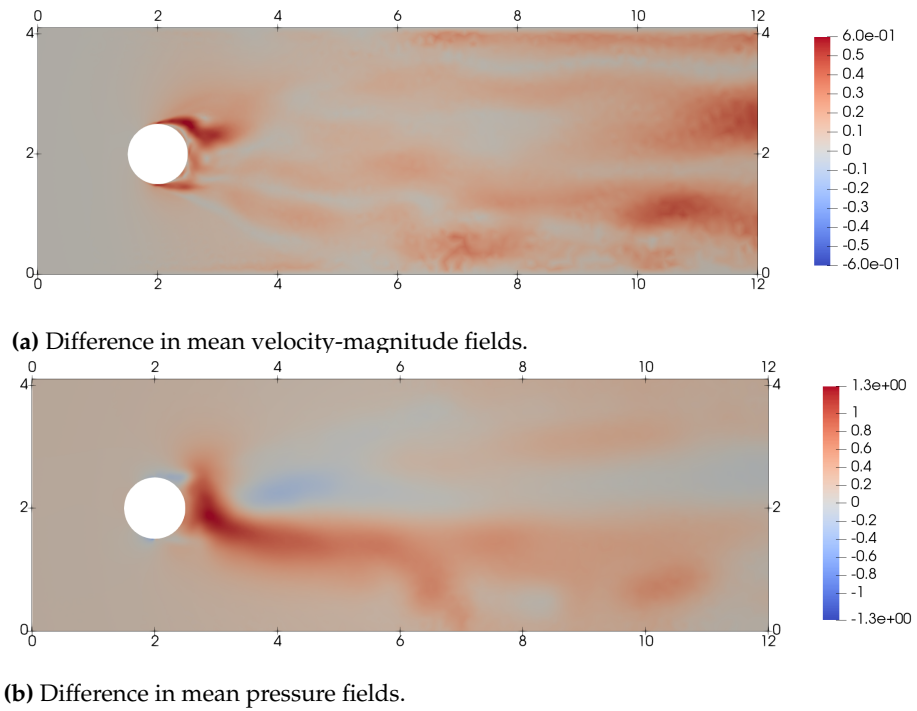


Figure 15. Difference in the mean flow fields at $Re = 2000$, between the controlled and baseline case.

This control strategy is completely different to that used low at lower Reynolds numbers of values $Re = 100$ and 1000 . In order to better understand this control strategy, a chronological velocity and pressure field snapshot is plotted in [Figure 16](#). In this case, the control strategy does not involve the elongation of the recirculation bubble behind the cylinder. The flow separation is controlled and energised by a high-frequency actuation of the jets. The separation point is moved behind the cylinder lowering the drag of the cylinder, similar to the Eiffel paradox phenomenon, also known as the drag crisis, as defined by Stabnikov and Garbaruk [47]. The agent tries to minimise the drag with this high frequency, breaking the vortices produced after the cylinder into smaller and less-energetic ones.

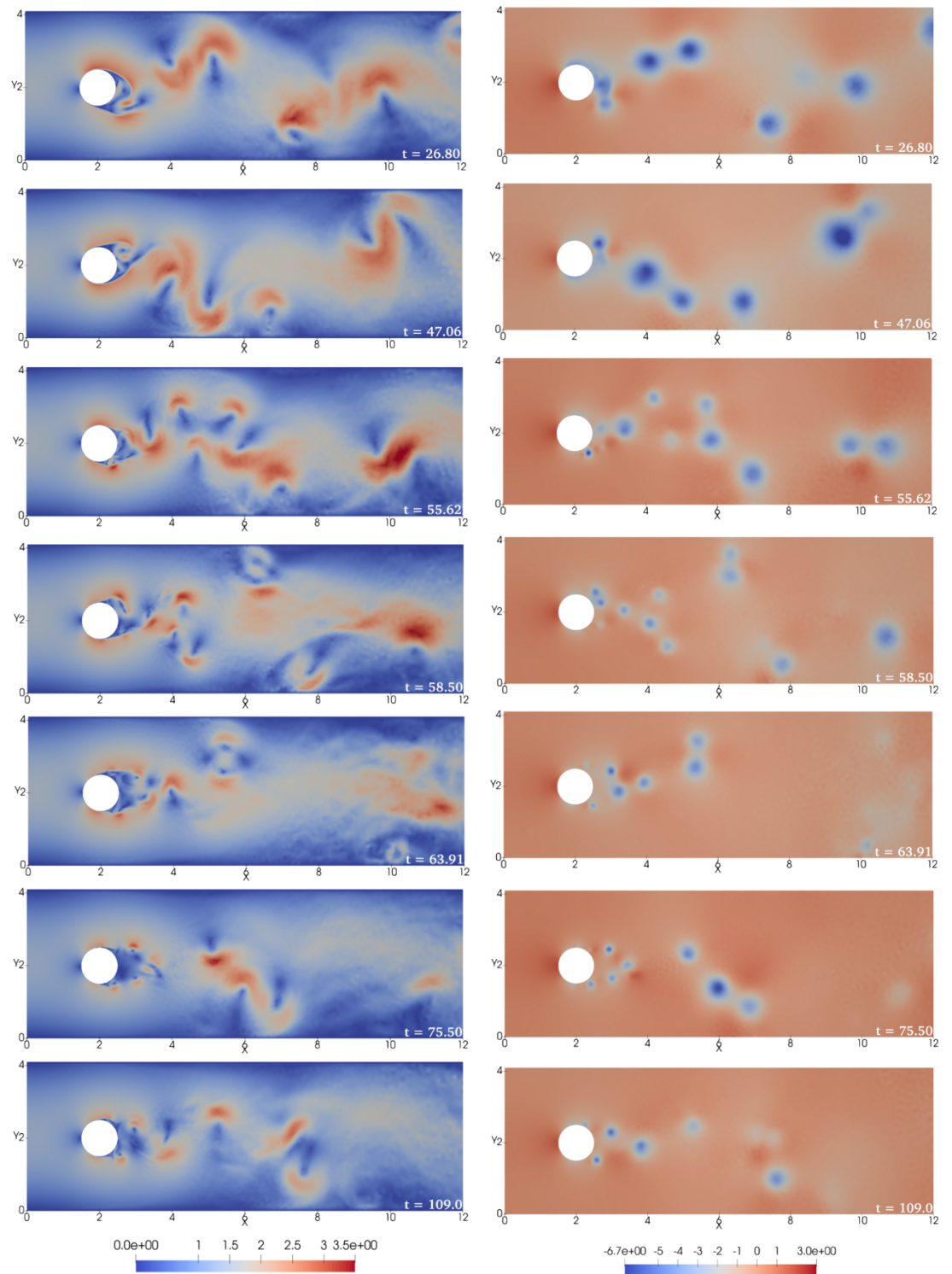


Figure 16. Velocity-magnitude (left) and pressure (right) fields progression at $Re = 2000$. The control starts at $t = 50$, therefore the first two panels of each column correspond to the uncontrolled case and the rest (involving smaller vortices) correspond to the controlled flow.

Additionally, one video of the velocity and pressure fields are shared to aid the visualisation. The corresponding link can be found at the end of the document in the "Data Availability Statement".

3.3. Cross-application of agents

Once the C_D improvement results have been obtained for all the calculated Reynolds numbers thanks to the use of DRL, the cross-application of agents for a flow at $Re = 2000$ is studied.

Cross-application of agents involves applying a previously trained ANN with a different Reynolds number flow to solve a similar problem, using the achieved learning in other conditions. The final objective is to reduce the computational cost of training the DRL agent, since training an ANN with a lower Reynolds number is less expensive. This approach can be very beneficial as long as the results produced by the agent are comparable, i.e. the physics are similar enough between the two different cases.

Here it is investigated the drag reduction obtained by the agents previously trained for Reynolds numbers 100 and 1000 when they are applied in a deterministic mode to the flow of $Re = 2000$, as can be seen in Figure 17.

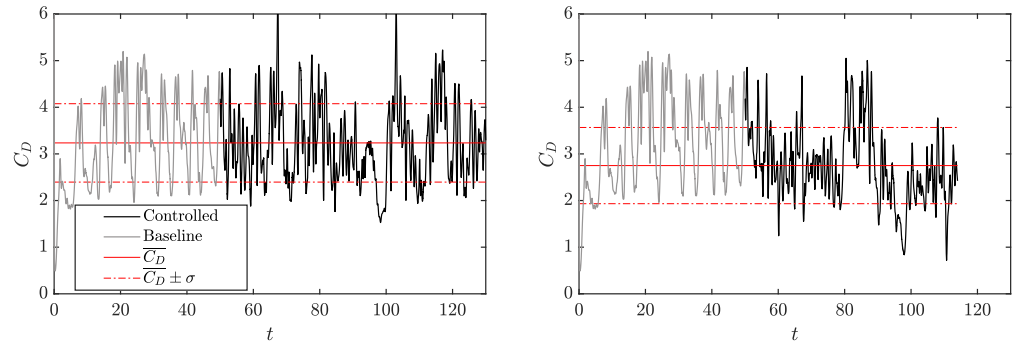


Figure 17. Temporal evolution of C_D obtained through cross-application of agents trained at $Re = 100$ (left) and $Re = 1000$ (right) in a deterministic mode to a case with a Reynolds number of 2000.

The cross-application of the agent trained at $Re = 100$ does not yield a result that reduces drag in a flow at $Re = 2000$. No drag improvement is obtained because the nature of the flow where the agent is applied is too different to the one where it was trained. However, when the trained agent at $Re = 1000$ is applied for the case of $Re = 2000$, a significant drag reduction is produced. An average C_D value of 2.74 is obtained, translating into a 19 % drag reduction improvement compared with the baseline flow. This is a slightly larger drag reduction to that obtained by the agent trained at $Re = 2000$. This small difference can be attributed to the chaotic nature of the flow, from evaluation run to evaluation run, and sub-optimal trade-off with respect to the actual reward function due to less good control of the lift and drag fluctuations, as will be discussed later. The fact that two similar results are obtained with different nature of control strategies, as explained in subsection 3.2, may indicate that the flow at $Re = 2000$ belongs to a transition regime towards a higher-Reynolds number flows which only admit a high-frequency control in order to obtain drag reduction. Therefore, being in this transition regime would admit both controls yielding comparable results. In order to go deep into this topic, higher Reynolds numbers must be simulated, but that goes beyond the scope of this article. At the same time, this is a doubly positive result since it confirms the fact that it is possible to apply deep-learning models previously trained at lower Reynolds number but

within the same Re regime (similar dynamics) while saving time and computational resources [48].

The average C_D comparisons for each agent used in the cross-application at $Re = 2000$ are shown in Figure 18 (left). As detailed in the previous section, the control strategy varies significantly as the Reynolds number increases. While at $Re = 100$ and 1000 , the control tries to keep the recirculation bubble behind the cylinder, at $Re = 2000$, high-frequency suction and blowing of the jets is applied to quickly force the flow transition, breaking the vortices into smaller ones. Despite these differences in the control strategies between the agents trained at $Re = 1000$ and 2000 , both are capable to obtain a comparable drag reduction in a flow at $Re = 2000$. As shown in Figure 18 (right), the C_L bias obtained using the policy from $Re = 1000$ is higher than that obtained using the policy of $Re = 2000$. Also, C_L fluctuations are larger when employing the agent trained at $Re = 1000$ (not shown here for the sake of brevity). Note that the $Re = 2000$ strategy reduces the drag almost as much as using cross-application of agents and, at the same time, exhibits a slightly better performance in the lift; since the lift is part of the reward function, the agent trained at $Re = 2000$ achieves a higher reward at $Re = 2000$ than the agent trained at $Re = 1000$. Nevertheless, the small differences between both trainings may be reversed for different baseline flows (changing the initial condition). This is similar to the results observed by Ren *et al.* [32].

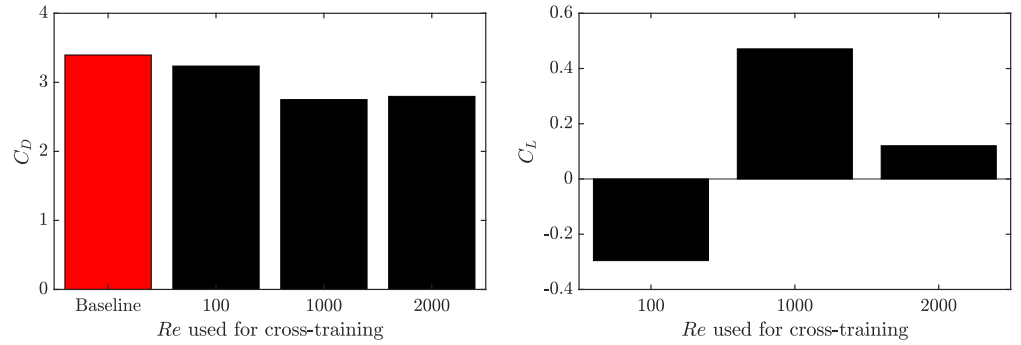


Figure 18. Average C_D (left) and average C_L (right) comparison between three different cross-application of agents.

In Figure 19, the average velocity-magnitude field at $Re = 2000$ is shown for the cross-application of the agent trained at $Re = 1000$. At first glance, it is noticeable the existent bias in the average velocity field, which is directly linked with the asymmetric lift behaviour.

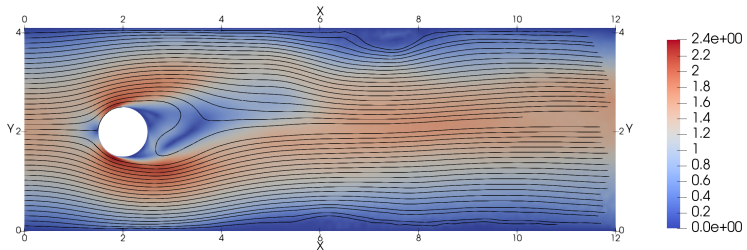


Figure 19. Average flow fields at $Re = 2000$, using the training obtained for $Re = 1000$.

In order to quantitatively observe the different control strategies, the power-spectral density (PSD) of the actions is plotted for the policy of $Re = 2000$, and the cross-application of agents, $Re = 1000$ and 100 , in Figure 20 (left). The latter two agents share the same strategy, which consist of a low-frequency action with no significant content at medium and high

frequencies. In contrast, with the policy of $Re = 2000$, the frequency spectrum is distributed, with a peak at a frequency of 1.1. In Figure 20 (right), the frequency spectrum of the pressure at the probe in the detachment region indicated in Figure 3 is shown. A low-frequency of 0.24 governs the baseline flow, corresponding to the vortex-shedding frequency. This frequency is mitigated by the policy of $Re = 2000$ in higher frequencies. Specifically, the frequency peak at 1.1 is a consequence of the corresponding actuations at this frequency, which is the responsible of breaking the flow into smaller vortices as seen in Figure 16. On the other hand, it can be seen how the agent trained at $Re = 1000$ tends towards a completely different strategy in terms of frequency, actuating with a low-frequency strategy. The agent trained at $Re = 100$, also uses this low-frequency actuation, but it does not have the capabilities to influence the pressure field. As mentioned before, in those cases, the agent tries an opposition control strategy increasing the recirculation bubble to minimise the drag.

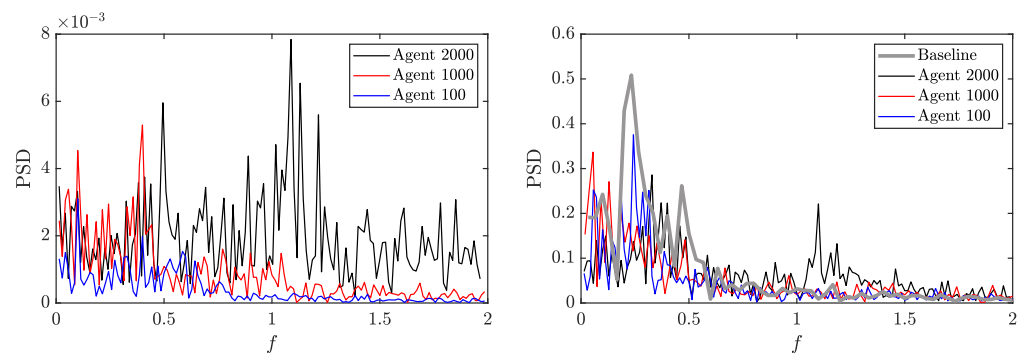


Figure 20. Power-spectral density the action output, Q , for the $Re = 2000$ case, with its own policy and two cross-application policies (left) and for pressure in the probe near the cylinder in the separation zone (right).

4. Conclusions

In this work, the high-performance CFD solver Alya has been coupled with an ANN DRL agent to simulate and control the flow around a 2D cylinder with two jets attached to the cylinder surface. The main control objective has been set on the reduction of the average drag. For the first time, the Reynolds number of the canonical 2D cylinder control problem from Rabault *et al.* [19] has been extended to $Re = 2000$, providing new insights into the DRL control strategies for highly complex and dynamical flows. Additionally, the $Re = 100$ and $Re = 1000$ cases have been studied for validation and comparison purposes.

The most striking outcome of case is that the DRL agent uses a radically different strategy from those obtained at lower Reynolds numbers while being able to provide a 17% drag reduction. In the new strategy, the agent tries to delay the detachment point in the cylinder surface using a high-frequency signal in the actuation of the jets, similarly to what can be observed in drag crisis phenomena. It is shown that the cylinder wake is narrowed by the breakdown of the detaching vortices into smaller structures. This strategy contrasts with the one obtained at a lower Reynolds number, where the agent acts at a lower frequency to perform opposition control and to elongate the recirculation bubble behind the cylinder. These results are further verified with the spectral analysis of the jet actuating signals and a pressure witness point in the wake.

Finally, the application of agents trained at $Re = 100$ and $Re = 1000$ on the $Re = 2000$ case has been investigated (namely cross-application). It has been shown that the $Re = 100$ agent is not able to reduce the drag in the high Reynolds regime, due to the different dynamics of the system. On the other hand, the $Re = 1000$ provides satisfactory results which even

beat the $Re = 2000$ agent itself (19% drag reduction), even though the mean wake displays an asymmetric pattern in this case, which corresponds to an overall reward (including lift bias penalisation) that is lower than with the agent trained at $Re = 2000$. Still, this opens the door to accelerate the training of an agent by first exposing it to a lower Reynolds-number flow, which demands a lower computational effort, and then finalise the training at the target Reynolds-number condition.

Author Contributions: Conceptualisation: RV, JR, OL; Investigation: all authors; Data curation: PV, PS, FAA, AM, JR, BF; Software: JR, AM, BF, OL; Writing original draft: PV, PS, FAA; Editing: all authors; Funding: LMGC, OL, RV. All authors have read and agreed to the published version of the manuscript.

Funding: Pau Varela is partially supported through a grant for the mobility of doctoral students provided by Universitat Politècnica de València and the program Erasmus Prácticas E+ 2020-1. RV acknowledges funding by the ERC through Grant No. “2021-CoG-101043998, DEEPCONTROL”.

Institutional Review Board Statement: Not applicable.

Informed Consent Statement: Not applicable.

Data Availability Statement: The data presented in this study are available on request from the corresponding author.

YouTube link to “Deep reinforcement learning for flow control on a cylinder a $Re=2,000$ ”:

<https://youtu.be/8R3adCQmeEA>

Acknowledgments: The authors acknowledge the contribution of Maxence Deferrez to this work. RV acknowledges funding by the ERC through Grant No. “2021-CoG-101043998, DEEPCONTROL”.

Conflicts of Interest: The authors declare no conflict of interest. The funders had no role in the design of the study; in the collection, analyses, or interpretation of data; in the writing of the manuscript, or in the decision to publish the results.

Abbreviations

The following abbreviations are used in this manuscript:

Abbreviations

AFC	Active flow control
ANN	Artificial neural network
BSC-CNS	Barcelona Supercomputing Center - Centro Nacional de Supercomputación
CFD	Computational fluid dynamics
CFL	Courant–Friedrichs–Lewy
CPU	Central processing unit
DRL	Deep reinforcement learning
EMAC	energy-, momentum- and angular-momentum-conserving equation
FEM	Finite-element method
HPC	High-performance computing
PPO	Proximal-policy optimisation
PSD	Power-spectral density
UAV	Unmanned aerial vehicle

Roman letters

a	action
C_L	Lift coefficient
C_D	Drag coefficient
C_{offset}	Offset coefficient of the reward
D	Cylinder diameter

e_j	Vector used in force calculation
f	External forces, frequency
f_k	Vortex shedding frequency
F	Force
F_D	Drag force
F_L	Lift Force
H	Channel height
L	Channel length
n	Unit vector normal to the cylinder
Q	Mass flow rate
Q^*	Normalised mass flow rate
Q_{ref}	Reference mass flow rate
p	Pressure
r	Reward
r_{norm}	Reference value of the reward after control
R	Cylinder radius
Re	Reynolds number
S	Surface
s	observation state
s_{norm}	Reference pressure in the observation state
St	Strouhal number
t	Time
t_0	Initial time
t_f	Final time
T_a	Action period
T_k	Vortex-shedding period
\mathbf{u}	Flow speed
\bar{U}	Mean velocity
U_{in}	Inlet boundary velocity in x direction
U_{max}	Inlet boundary velocity in the middle of the channel
V_{in}	Inlet boundary velocity in y direction
v_i	Jet velocity
w	Lift penalisation
x	Horizontal coordinate
y	Vertical coordinate

Greek letters

ϵ	Velocity strain-rate tensor
ν	Kinematic viscosity
Ω	Domain
ω	Jet angular opening
ρ	Density
σ	Standard deviation
ζ	Cauchy stress tensor
θ	Jet angle
θ_0	Centre jet angle

References

1. Howell, J.P. *Aerodynamic drag reduction for low carbon vehicles*; Woodhead Publishing Limited, **2012**; pp. 145–154. doi:10.1533/9780857094575.4.145
2. Bechert, D.W.; Bartenwerfer, M. The viscous flow on surfaces with longitudinal ribs. *Journal of Fluid Mechanics* **1989**, *206*, 105–129. doi:10.1017/S0022112089002247.
3. Gad-el Hak, M. *Active, and Reactive Flow Management*. Cambridge University Press, England; **2000**. doi:10.1017/CBO9780511529535.

4. Guerrero, J.; Sanguineti, M.; Wittkowski, K. CFD Study of the Impact of Variable Cant Angle Winglets on Total Drag Reduction. *Aerospace* **2018**, *5*, 126. doi:10.3390/aerospace5040126.
5. Tiseira, A.O.; García-Cuevas, L.M.; Quintero, P.; Varela, P. Series-hybridisation, distributed electric propulsion and boundary layer ingestion in long-endurance, small remotely piloted aircraft: Fuel consumption improvements. *Aerospace Science and Technology* **2022**, *120*, 107227. doi:10.1016/j.ast.2021.107227.
6. Serrano, J.R.; García-Cuevas, L.M.; Bares Moreno, P.; Varela Martínez, P. Propeller Position Effects over the Pressure and Friction Coefficients over the Wing of an UAV with Distributed Electric Propulsion: A Proper Orthogonal Decomposition Analysis. *Drones* **2022**, *6*, 38. doi:10.3390/drones6020038.
7. Serrano, J.R.; Tiseira, A.O.; García-Cuevas, L.M.; Varela, P. Computational Study of the Propeller Position Effects in Wing-Mounted, Distributed Electric Propulsion with Boundary Layer Ingestion in a 25 kg Remotely Piloted Aircraft. *Drones* **2021**, *5*, 56. doi:10.3390/drones5030056.
8. Kametani, Y.; Fukagata, K. Direct numerical simulation of spatially developing turbulent boundary layers with uniform blowing or suction. *Journal of Fluid Mechanics* **2011**, *681*, 154–172. doi:10.1017/jfm.2011.219.
9. Fan, Y.; Atzori, M.; Vinuesa, R.; Gatti, D.; Schlatter, P.; Li, W. Decomposition of the mean friction drag on an NACA4412 airfoil under uniform blowing/suction. *Journal of Fluid Mechanics* **2022**, *932*, A31. doi:10.1017/jfm.2021.1015.
10. Atzori, M.; Vinuesa, R.; Schlatter, P. Control effects on coherent structures in a non-uniform adverse-pressure-gradient boundary layer. *International Journal of Heat and Fluid Flow* **2022**, *97*, 109036. doi:https://doi.org/10.1016/j.ijheatfluidflow.2022.109036.
11. Atzori, M.; Vinuesa, R.; Stroh, A.; Gatti, D.; Frohnafel, B.; Schlatter, P. Uniform blowing and suction applied to nonuniform adverse-pressure-gradient wing boundary layers. *Phys. Rev. Fluids* **2021**, *6*, 113904. doi:10.1103/PhysRevFluids.6.113904.
12. Fahland, G.; Stroh, A.; Frohnafel, B.; Atzori, M.; Vinuesa, R.; Schlatter, P.; Gatti, D. Investigation of Blowing and Suction for Turbulent Flow Control on Airfoils. *AIAA Journal* **2021**, p. 1–15. doi:10.2514/1.J060211.
13. Voevodin, A.V.; Korniyakov, A.A.; Petrov, A.S.; Petrov, D.A.; Sudakov, G.G. Improvement of the take-off and landing characteristics of wing using an ejector pump. *Thermophysics and Aeromechanics* **2019**, *26*, 9–18. doi:10.1134/S0869864319010025.
14. Yousefi, K.; Saleh, R. Three-dimensional suction flow control and suction jet length optimization of NACA 0012 wing. *Meccanica* **2015**, *50*, 1481–1494. doi:10.1007/s11012-015-0100-9.
15. Cui, W.; Zhu, H.; Xia, C.; Yang, Z. *Comparison of Steady Blowing and Synthetic Jets for Aerodynamic Drag Reduction of a Simplified Vehicle*; Vol. 126, Elsevier B.V., **2015**; pp. 388–392. doi:10.1016/j.proeng.2015.11.224.
16. Park, H.; Cho, J.H.; Lee, J.; Lee, D.H.; Kim, K.H. Experimental study on synthetic jet array for aerodynamic drag reduction of a simplified car.
17. Choi, H.; Moin, P.; Kim, J. Active turbulence control for drag reduction in wall-bounded flows. *Journal of Fluid Mechanics* **1994**, *262*, 75–110. doi:10.1017/S0022112094000431.
18. Muddada, S.; Patnaik, B.S. An active flow control strategy for the suppression of vortex structures behind a circular cylinder. *European Journal of Mechanics, B/Fluids* **2010**, *29*, 93–104. doi:10.1016/j.euromechflu.2009.11.002.
19. Rabault, J.; Kuchta, M.; Jensen, A.; Réglade, U.; Cerardi, N. Artificial neural networks trained through deep reinforcement learning discover control strategies for active flow control. *Journal of Fluid Mechanics* **2019**, *865*, 281–302, [1808.07664]. doi:10.1017/jfm.2019.62.
20. Ghraieb, H.; Viquerat, J.; Larcher, A.; Meliga, P.; Hachem, E. Optimization and passive flow control using single-step deep reinforcement learning. *Physical Review Fluids* **2021**, *6*, [2006.02979]. doi:10.1103/PhysRevFluids.6.053902.
21. Pino, F.; Schena, L.; Rabault, J.; Mendez, M. Comparative analysis of machine learning methods for active flow control. *arXiv preprint arXiv:2202.11664* **2022**.
22. Garnier, P.; Viquerat, J.; Rabault, J.; Larcher, A.; Kuhnle, A.; Hachem, E. A review on deep reinforcement learning for fluid mechanics. *Computers and Fluids* **2021**, *225*, [1908.04127]. doi:10.1016/j.compfluid.2021.104973.
23. Rabault, J.; Ren, F.; Zhang, W.; Tang, H.; Xu, H. Deep reinforcement learning in fluid mechanics: A promising method for both active flow control and shape optimization. *Journal of Hydrodynamics* **2020**, *32*, 234–246.
24. Vinuesa, R.; Brunton, S.L. Enhancing computational fluid dynamics with machine learning. *Nature Computational Science* **2022**, *2*, 358–366. doi:10.1038/s43588-022-00264-7.
25. Vinuesa, R.; Lehmkühl, O.; Lozano-Durán, A.; Rabault, J. Flow Control in Wings and Discovery of Novel Approaches via Deep Reinforcement Learning. *Fluids* **2022**, *7*. doi:10.3390/fluids7020062.
26. Belus, V.; Rabault, J.; Viquerat, J.; Che, Z.; Hachem, E.; Reglade, U. Exploiting locality and translational invariance to design effective deep reinforcement learning control of the 1-dimensional unstable falling liquid film. *AIP Advances* **2019**, *9*. doi:10.1063/1.5132378.
27. Rabault, J.; Kuhnle, A. Accelerating deep reinforcement learning strategies of flow control through a multi-environment approach. *Physics of Fluids* **2019**, *31*, [1906.10382]. doi:10.1063/1.5116415.
28. Tang, H.; Rabault, J.; Kuhnle, A.; Wang, Y.; Wang, T. Robust active flow control over a range of Reynolds numbers using an artificial neural network trained through deep reinforcement learning. *Physics of Fluids* **2020**, *32*, 1–15, [2004.12417]. doi:10.1063/5.0006492.
29. Tokarev, M.; Palkin, E.; Mullyadzhannov, R. Deep reinforcement learning control of cylinder flow using rotary oscillations at low Reynolds number. *Energies* **2020**, *13*, 1–11. doi:10.3390/en13225920.

30. Xu, H.; Zhang, W.; Deng, J.; Rabault, J. Active flow control with rotating cylinders by an artificial neural network trained by deep reinforcement learning. *Journal of Hydrodynamics* **2020**, *32*, 254–258.
31. Li, J.; Zhang, M. Reinforcement-learning-based control of confined cylinder wakes with stability analyses. *Journal of Fluid Mechanics* **2022**, *932*, 1–35, [2111.07498]. doi:10.1017/jfm.2021.1045.
32. Ren, F.; Rabault, J.; Tang, H. Applying deep reinforcement learning to active flow control in weakly turbulent conditions. *Physics of Fluids* **2021**, *33*, [2006.10683]. doi:10.1063/5.0037371.
33. Wang, Q.; Yan, L.; Hu, G.; Li, C.; Xiao, Y.; Xiong, H.; Rabault, J.; Noack, B.R. DRLinFluids: An open-source Python platform of coupling deep reinforcement learning and OpenFOAM. *Physics of Fluids* **2022**, *34*, 081801, [https://doi.org/10.1063/5.0103113]. doi:10.1063/5.0103113.
34. Qin, S.; Wang, S.; Rabault, J.; Sun, G. An application of data driven reward of deep reinforcement learning by dynamic mode decomposition in active flow control. *arXiv preprint arXiv:2106.06176* **2021**.
35. Vazquez, M.; Houzeaux, G.; Koric, S.; Artigues, A.; Aguado-Sierra, J.; Aris, R.; Mira, D.; Calmet, H.; Cucchietti, F.; Owen, H.; Taha, A.; Cela, J.M. Alya: Towards Exascale for Engineering Simulation Codes **2014**. [1404.4881].
36. Owen, H.; Houzeaux, G.; Samaniego, C.; Lesage, A.C.; Vázquez, M. Recent ship hydrodynamics developments in the parallel two-fluid flow solver Alya. *Computers and Fluids* **2013**, *80*, 168–177. doi:10.1016/j.compfluid.2012.03.022.
37. Lehmkuhl, O.; Houzeaux, G.; Owen, H.; Chrysokentis, G.; Rodriguez, I. A low-dissipation finite element scheme for scale resolving simulations of turbulent flows. *Journal of Computational Physics* **2019**, *390*, 51–65. doi:10.1016/j.jcp.2019.04.004.
38. Charnyi, S.; Heister, T.; Olshanskii, M.A.; Rebholz, L.G. On conservation laws of Navier–Stokes Galerkin discretizations. *Journal of Computational Physics* **2017**, *337*, 289–308, [1605.09763]. doi:10.1016/j.jcp.2017.02.039.
39. Charnyi, S.; Heister, T.; Olshanskii, M.A.; Rebholz, L.G. Efficient discretizations for the EMAC formulation of the incompressible Navier–Stokes equations. *Applied Numerical Mathematics* **2019**, *141*, 220–233, [1712.00857]. doi:10.1016/j.apnum.2018.11.013.
40. Crank, J.; Nicolson, P. A practical method for numerical evaluation of solutions of partial differential equations of the heat-conduction type. *Advances in Computational Mathematics* **1996**, *6*, 207–226. doi:10.1007/bf02127704.
41. Trias, F.X.; Lehmkuhl, O. A self-adaptive strategy for the time integration of navier-stokes equations. *Numerical Heat Transfer, Part B: Fundamentals* **2011**, *60*, 116–134. doi:10.1080/10407790.2011.594398.
42. Kuhnle, A.; Schaarschmidt, M.; Fricke, K. Tensorforce: a TensorFlow library for applied reinforcement learning. Web page, **2017**.
43. Abadi, M.; Agarwal, A.; Barham, P.; Brevdo, E.; Chen, Z.; Citro, C.; Corrado, G.S.; Davis, A.; Dean, J.; Devin, M.; Ghemawat, S.; Goodfellow, I.; Harp, A.; Irving, G.; Isard, M.; Jia, Y.; Jozefowicz, R.; Kaiser, L.; Kudlur, M.; Levenberg, J.; Mané, D.; Monga, R.; Moore, S.; Murray, D.; Olah, C.; Schuster, M.; Shlens, J.; Steiner, B.; Sutskever, I.; Talwar, K.; Tucker, P.; Vanhoucke, V.; Vasudevan, V.; Viégas, F.; Vinyals, O.; Warden, P.; Wattenberg, M.; Wicke, M.; Yu, Y.; Zheng, X. TensorFlow: Large-Scale Machine Learning on Heterogeneous Systems, **2015**. Software available from tensorflow.org.
44. Schäfer, M.; Turek, S.; Durst, F.; Krause, E.; Rannacher, R. *Benchmark Computations of Laminar Flow Around a Cylinder*; Vieweg+Teubner Verlag: Wiesbaden, **1996**; pp. 547–566. doi:10.1007/978-3-322-89849-4_39.
45. Elhawary, M. Deep reinforcement learning for active flow control around a circular cylinder using unsteady-mode plasma actuators. *arXiv* **2020**, pp. 1–19.
46. Han, B.Z.; Huang, W.X.; Xu, C.X. Deep reinforcement learning for active control of flow over a circular cylinder with rotational oscillations. *International Journal of Heat and Fluid Flow* **2022**, *96*, 109008. doi:10.1016/j.ijheatfluidflow.2022.109008.
47. Stabnikov, A.; Garbaruk, A. Prediction of drag crisis on a circular cylinder using a new algebraic transition model coupled with SST DDES. *Journal of Physics: Conference Series* **2020**, *1697*, 012224. doi:10.1088/1742-6596/1697/1/012224.
48. Guastoni, L.; Güemes, A.; Ianiro, A.; Discetti, S.; Schlatter, P.; Azizpour, H.; Vinuesa, R. Convolutional-network models to predict wall-bounded turbulence from wall quantities. *Journal of Fluid Mechanics* **2021**, *928*, A27. doi:10.1017/jfm.2021.812.